

Nanocrystalline Titanium Metal–Organic Frameworks for Highly Efficient and Flexible Perovskite Solar Cells

UnJin Ryu,[†] Seohyeon Jee,[†] Joon-Suh Park,[‡] Il Ki Han,[‡] Ju Ho Lee,[§] Minwoo Park,^{*,†} and Kyung Min Choi^{*,†}

[†]Department of Chemical and Biological Engineering, Sookmyung Women's University, Seoul 04310, Korea

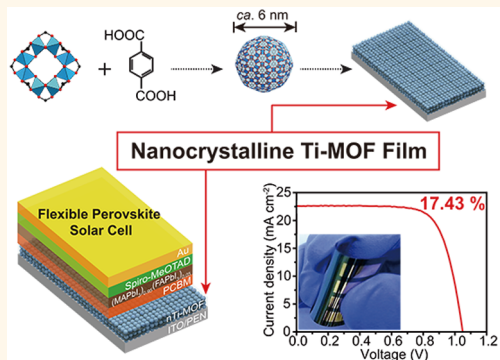
[‡]Nanophotonics Research Center, Korea Institute of Science and Technology (KIST), Seoul 02792, Korea

[§]Reliability Research Center, Korea Electronics Technology Institute (KETI), 25 Saenari-ro, Bundang-gu, Seongnam-si, Gyeonggi-do 463-816, South Korea

Supporting Information

ABSTRACT: Flexible perovskite solar cells (PSCs) have attracted considerable attention due to their excellent performance, low-cost, and great potential as an energy supplier for soft electronic devices. In particular, the design of charge transporting layers (CTLs) is crucial to the development of highly efficient and flexible PSCs. Herein, nanocrystalline Ti-based metal–organic framework (nTi-MOF) particles are synthesized to have *ca.* 6 nm in diameter. These are then well-dispersed in alcohol solvents in order to generate electron transporting layers (ETLs) in PSCs under ambient temperatures using a spin-coating process. The electronic structure of nTi-MOF ETL is found to be suitable for charge injection and transfer from the perovskite to the electrodes. The combination of a [6,6]-phenyl-C₆₁-butyric acid (PCBM) into the nTi-MOF ETL provides for efficient electron transfer and also suppresses direct contact between the perovskite and the electrode. This results in impressive power conversion efficiencies (PCEs) of 18.94% and 17.43% for rigid and flexible devices, respectively. Moreover, outstanding mechanical stability is retained after 700 bending cycles at a bending radius (*r*) of 10 mm.

KEYWORDS: metal–organic frameworks, nanocrystals, titanium oxo-cluster, flexible perovskite solar cells, electron transporting layers



In recent years, remarkable developments in metal halide perovskite solar cells (PSCs) have been presented in the field of photovoltaics.^{1–3} Solution-processable perovskite materials, with excellent optoelectronic properties, have boosted the power conversion efficiency (PCE) of the devices to 22.7%.⁴ The outstanding mechanical flexibility of perovskites makes them a feasible energy supplier for both wearable devices and building integrated photovoltaic (BIPV) systems.^{5–7} For highly efficient and flexible devices, the electrical and optical properties of charge transporting layers (CTLs) are crucial as they determine charge injection and transfer behavior in the device.^{8–14} In particular, metal oxides are a promising material, since they have excellent carrier mobility and environmental stability.^{15–17} Synthetic metal oxide nanostructure protocols have been suggested for preparing efficient CTL for use in flexible PSCs. For example, NiO_x hole transporting layers have been prepared using simple sol–gel and combustion methods. This produced rigid and flexible devices, which exhibited impressive PCEs of 17.6% and 14.53%, respectively.^{18,19}

Colloidal Zn₂SnO₄ also showed great potential for use in flexible PSCs, producing PCEs that exceeded 16%.²⁰

In metal oxide-based PSCs, high PCEs occur in the devices employing TiO₂ electron transporting layers (ETLs). The mesoporous TiO₂ ETL provides a large contact area between the TiO₂ and perovskite. However, a high annealing temperature (>450 °C) is required to fabricate TiO₂ ETLs, and this has been a critical barrier for their application to flexible architecture. Even if chlorine-capped TiO₂ nanocrystal was recently introduced at a relatively low annealing temperature of 150 °C,²¹ the temperature is still too high to build-up flexible PSCs on plastic substrates. Therefore, a room-temperature process has been sought-after technology. In a previous study, TiO_x ETLs fabricated *via* atomic layer deposition led to excellent PCEs (12–15%) and device flexibility.^{12,13} However,

Received: March 20, 2018

Accepted: May 4, 2018

Published: May 4, 2018

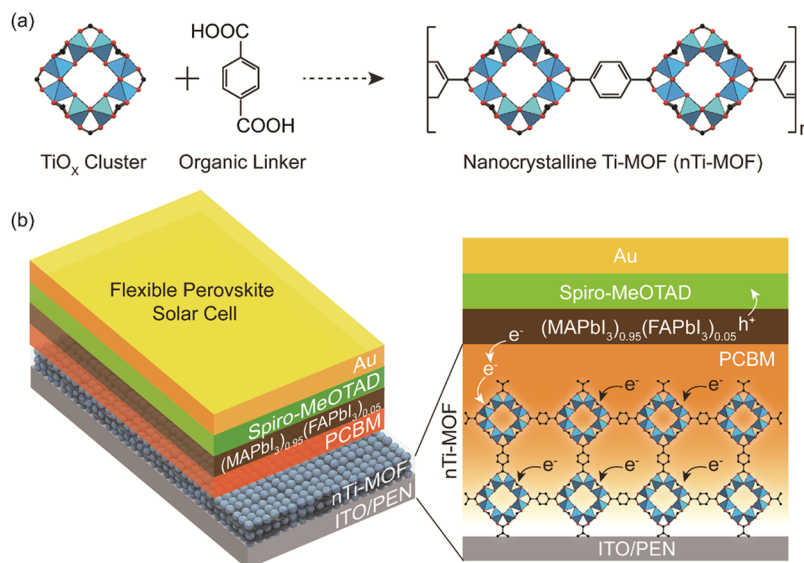


Figure 1. (a) Schematic of the synthetic protocol for nanocrystalline Ti-MOF (nTi-MOF). The successive linked TiO_2 clusters with BDC molecules create small nanocrystals. (b) Device structure of a flexible perovskite solar cell incorporating nTi-MOF/PCBM ETL. The magnified image indicates electron and hole transfer from the perovskite toward interlayers, nTi-MOF/PCBM, and spiro-MeOTAD, respectively.

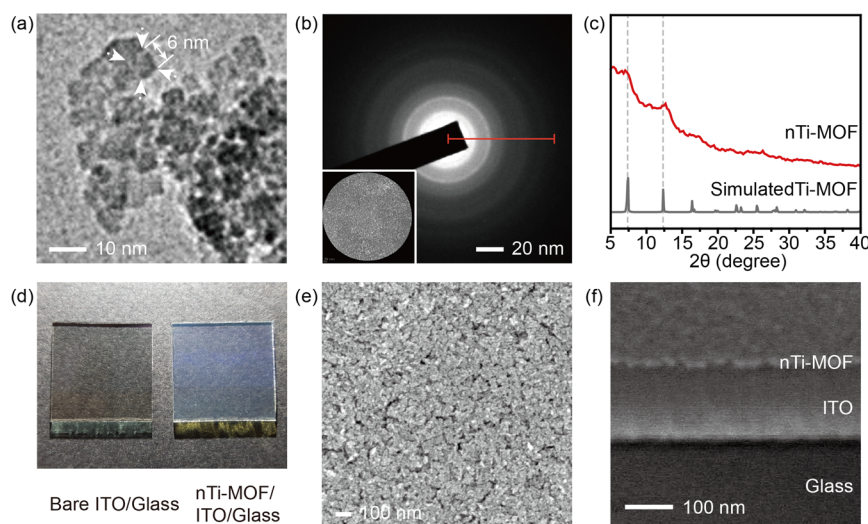


Figure 2. (a) TEM image of a synthesized nTi-MOF. (b) The selected area electron diffraction (SAED) corresponding to the inset TEM image. (c) Converted XRD patterns of the nTi-MOFs from SAED. (d) Photograph of a bare ITO/glass (left) and a nTi-MOF/ITO/glass (right). (e, f) SEM image of the nTi-MOF ETL deposited onto an ITO/glass substrate obtained by (e) the top view and (f) the cross-section view.

this method requires a vacuum. Intense pulsed light sintering was used for ultrafast processing time of both compact and mesoporous TiO_2 ETLs to give PCEs of 11.2%²² and 12%. In other studies, chlorine-capped TiO_2 nanocrystal was introduced to fabricate PSCs. Recently, a photosintering method, using ultraviolet (UV) radiation to produce TiO_2 nanocrystal films created ultrathin, highly crystalline, and pinhole-free TiO_2 ETLs. These exhibited an improved PCE (16.01%) and were easier to process (processing temperature of ETLs <50 °C).¹⁴ However, the long UV exposure times (>4 h) posed a challenge.

The design of TiO_2 nanostructures can be derived from the smallest titanium oxide units that are spatially linked together. This is expected to allow flexible and high-performance PSCs to be made using a fast process, and under room-temperature

conditions. In this context, Ti-based metal–organic frameworks (Ti-MOFs) are an ideal candidate, as they are well-ordered materials, constructed by stitching Ti oxo-cluster and organic linkers together (Figure 1a).^{24,25} In this report, we choose MIL-125(Ti) composed of a titanium oxocarboxo cluster $[\text{Ti}_8\text{O}_8(\text{OH})_4(-\text{COO})_6]$ cross-linked with a 1,4-benzenedicarboxylate (BDC) linker.^{26–28} Their nanocrystalline form can enhance the film uniformity in the ETL of a flexible PSC, and the solution processability is compatible with perovskite materials. Therefore, the Ti-MOF in this research was synthesized in nanocrystalline form so that the diameter is *ca.* 6 nm (hereafter, this nanocrystalline MIL-125(Ti) is termed nTi-MOF). The ultrathin and uniform nTi-MOF ETLs are fabricated onto an indium tin oxide (ITO)/polyethylene naphthalate (PEN) substrate, using spin coating from the

nTi-MOF colloidal dispersion. The operation of the device follows the conventional n-i-p planar heterojunction structure employing a lead triiodide perovskite, comprising mixed cations of methylammonium and formamidinium, $(\text{MAPbI}_3)_{0.95}(\text{FAPbI}_3)_{0.05}$ (Figure 1b). The nTi-MOF/PCBM hybrid ETL (PCBM = [6,6]-phenyl-C₆₁-butyric acid) provides an excellent PCE of 18.94% and 17.43% for rigid and flexible devices, respectively. To the best of our knowledge, our devices show the best performance among all TiO₂-based flexible PSCs.

There are two other studies using MOFs in PSCs. In the first, Zr-based porphyrin MOF (MOF-525) nanocrystals were incorporated into a perovskite layer as an additive (5 v/v %). This gave an average PCE of 12.0%.²⁹ In the second, TiO₂ nanoparticles are composited with 3% of MIL-125, to produce a depleted perovskite/TiO₂-MOF heterojunction solar cell, with a PCE of 6.4%.³⁰ The present study is the first case to replace TiO₂ nanoparticles using nanocrystalline MOFs in ETLs, which produces the highest PCE of 18.94%. This PCE is significantly higher than all other studies using MOFs for all classes of solar cells including PSCs (3–13%).³¹

RESULTS AND DISCUSSION

Samples of nTi-MOF particles were prepared by solvothermal synthesis. The 1,4-benzenedicarboxylic acid (H₂BDC) was dissolved in a mixture of anhydrous DMF and methanol using ultrasonication, in a 20 mL Teflon-lined vial. Then, titanium(IV) butoxide was added to this solution and fully dissolved by stirring vigorously for 30 min at room temperature. The solution was sealed and heated at 150 °C for 15 h using an aluminum heating block. The white suspensions thus produced were collected and washed three times with DMF, using a centrifuge. They were then sequentially immersed in methanol for three 24 h periods. The nTi-MOF particles were separated using a centrifuge and then dried *in vacuo* overnight for further characterization. Transmission electron microscopy (TEM) of the product showed angular-shaped crystals with an average size of 6 nm (Figure 2a). Diffraction rings in Figure 2b show the result of Bragg scattering as the electron beam passes through the particles shown in the inset of Figure 2b, which indicates that the nTi-MOF particles are crystalline. The intensity profile of the diffraction rings was converted into 2-θ scale and compared with that of a simulated pattern obtained using experimental X-ray single-crystal diffraction data (Figure 2c).²⁶ The coincidence of the diffraction lines between nTi-MOF and simulated Ti-MOF indicates preservation of the bulk Ti-MOF structure arrangement for nTi-MOF particles. The IR spectroscopy of the nTi-MOF particles shows Ti–O stretching vibrations similar to the bulk Ti-MOF, which indicates that the organic and inorganic parts and their bonding in both samples are similar (Figure S1). However, the stronger conjugated C=O stretch in nTi-MOF than that in bulk Ti-MOF indicates the existence of the coordinated-free carboxylic groups as dangling bond on the surface of nTi-MOF particles. The XPS data show that both nTi-MOF and bulk Ti-MOF samples have identical binding energies of Ti 2p (458.2 and 464.0 eV), C 1s (284.4, 285.9, and 288.5 eV), and O 1s (529.9, 531.5, and 533.1 eV) and similar elemental ratios (Figure S2). The permanent porosity was confirmed by measuring the nitrogen gas sorption isotherm (Figure S3). It shows microporous sorption at low pressures ($0 < P/P_0 < 0.05$) and additional sorption in higher pressure areas due to the interparticle space. We speculate that the most important factor to give such small-sized nanocrystals is high rates of heat transfer from aluminum heating block

which thermal conductivity is 273 W m⁻¹ k⁻¹. In conventional MOF synthesis, a convection oven is commonly used, and the thermal conductivity of the air in it is only 0.024 W m⁻¹ k⁻¹. We have synthesized the Ti-MOF in the convection oven under identical temperature and got large crystals over a few hundred nanometers (Figure S4). The small-sized nanocrystals are advantageous for the solution-based film fabrication process described in the next step. This is because they can be used to make colloidal dispersions in most organic and alcohol solvents without aggregation (Figure S5).

The nTi-MOF ETLs were fabricated using a spin coating of the colloidal solution. Figure 2d shows photographs of an ITO/glass and a nTi-MOF/ITO/glass. A pale milky color was observed after formation of the nTi-MOF film, and this exhibited a high optical transparency of 97.7% at 550 nm (Figure S6). Figure 2e,f shows scanning electron microscope (SEM) images of the nTi-MOF ETL (top and side views, respectively). From Figure 2f, the film thickness is found to be around 20 nm, which indicates that a triple-layered nTi-MOF was formed. Because microcracks were observed in the nTi-MOF ETLs (Figure 2e), the PCBM was covered during the PSC fabrication process to avoid direct contact between the perovskite and ITO (as shown in Figure S7).

X-ray photoelectron spectroscopy (XPS), ultraviolet-visible (UV-vis) spectra, and ultraviolet photoelectron spectroscopy (UPS) were thoroughly investigated in order to elucidate the chemical state and electronic structure of the nTi-MOFs. These were compared with those of anatase TiO₂ nanoparticles (diameter = 20 nm). Figure 3a shows the XPS spectra of the

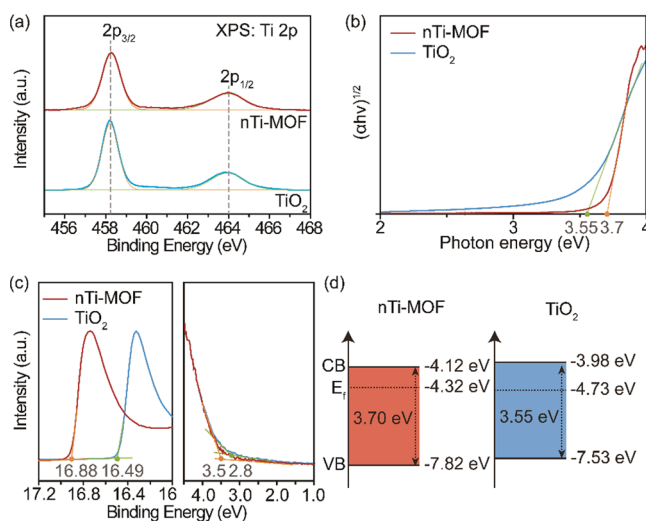


Figure 3. (a) XPS spectra of the nTi-MOF ETL and mesoporous TiO₂ ETL. (b) Tauc plots of the nTi-MOF ETL and mesoporous TiO₂ ETL. These were obtained from UV-vis spectra. (c) UPS spectra of the nTi-MOF ETL and mesoporous TiO₂ ETL. (d) Energy diagrams of the nTi-MOF (left) and the TiO₂ nanoparticle (right) obtained from the calculation of energy levels and E_g.

nTi-MOFs and TiO₂ nanoparticles. The spectra were calibrated by centering the C 1s peak at 284.8 eV. The Ti 2p_{3/2} and Ti 2p_{1/2} peaks of the nTi-MOFs were found to be 458.2 and 464.0 eV, respectively. These correspond to those of the TiO₂ nanoparticles. This suggests that the chemical state of Ti in the Ti-MOFs is almost similar to that of Ti in TiO₂ nanoparticles. The electronic structures of the nTi-MOFs, however, were slightly different from that found in TiO₂

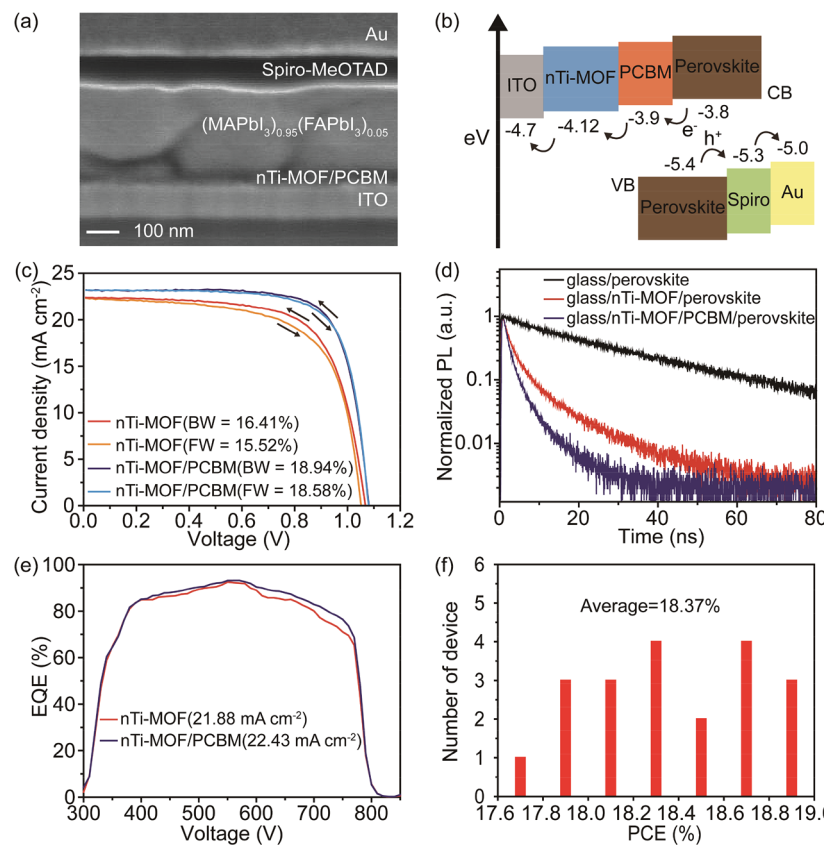


Figure 4. Characterization of the rigid nTi-MOF/PCBM PSCs. (a) Cross-section SEM image of the device. The sample for SEM analysis was prepared using a focused ion beam (FIB). (b) Energy diagram of the deposited layers, indicating the electron and hole transfer from the perovskite to the respective layers. (c) J – V curves of nTi-MOF device and nTi-MOF/PCBM device. The arrows indicate the directions of voltage sweeps. (d) Time-resolved PL spectra of the three samples: glass/perov, glass/nTi-MOF/perov, and glass/nTi-MOF/PCBM/perov. (e) EQE spectra of the nTi-MOF device and the nTi-MOF/PCBM device. (f) Histogram of the PCEs for 20 devices.

nanostructures. The Tauc plot in Figure 3b clearly shows that the band gap (E_g) of the nTi-MOFs is 3.7 eV. This is broader than that found in the TiO_2 nanoparticles ($E_g = 3.55$ eV). The UPS spectra of the nTi-MOFs and TiO_2 nanoparticles exhibit different binding energies for both low- and high-energy regimes (Figure 3c). Using the values of the cutoff binding energy (E_{cutoff}), Fermi edge ($E_{\text{F,edge}}$), and Fermi level (E_F) in the UPS spectra, the conduction band minimum (CBM) and valence band maximum (VBM) of the nTi-MOFs were calculated to be -4.12 eV and -7.82 eV, respectively (Figure 3d). Those of the TiO_2 nanoparticles were calculated to be -3.98 eV and -7.53 eV, respectively (Figure 3d). Considering that CBM of perovskite layer is -3.80 eV, the electronic structures of the nTi-MOFs are suitable for charge injection and transfer from the perovskite to the electrodes. The electrical conductivity of the nTi-MOF ETL (4.46×10^{-5} S cm $^{-1}$) was slightly lower than that of the TiO_2 ETL (6.38×10^{-5} S cm $^{-1}$) and depended on the film thickness. The conductivity of nTi-MOF ETLs significantly decreased from 4.46×10^{-5} S cm $^{-1}$ to 2.32×10^{-5} S cm $^{-1}$ as the film thickness increased from 20 to 60 nm, which was attributed to the increasing contact resistance between the nTi-MOFs (Figure S8). However, it should be noted that the conductivity of the nTi-MOF ETLs was significantly enhanced up to 1.09×10^{-4} S cm $^{-1}$ after deposition of PCBM (Figure S8). This is because PCBM provides electrical pathways by filling the microcracks within the nTi-MOF ETL. In this regard, the incorporation of PCBM into the nTi-MOF ETL is beneficial, as it improves its

conductivity and suppresses direct contact between the perovskite and ITO.

The next stage was to employ the nTi-MOF/PCBM ETLs in the PSCs, in order to make an nTi-MOF/PCBM device. Figure 4a shows a cross-sectional SEM of the device architecture. A 450 nm-thick, and pinhole-free, perovskite layer was deposited onto the 50 nm-thick nTi-MOF/PCBM ETL using the Lewis base adduct method (Figure S9).³² A small amount of formamidinium iodide (FAI) was added, and UV-vis spectra of the perovskites showed that the cutoff wavelength underwent a redshift from 780 to 800 nm, as a result (Figure S10). A 200 nm-thick spiro-MeOTAD was deposited onto the perovskite, and then Au contacts were deposited using a thermal evaporator. The energy diagram of the device in Figure 4b shows the charge transfer from the perovskite to the respective layer. The nTi-MOF ETLs without a PCBM layer were also used to make PSCs (nTi-MOF devices), and these were compared with the nTi-MOF/PCBM devices. Figure 4c shows the photocurrent density–voltage (J – V) curves of the devices. At a scan delay time of 200 ms, the PCEs of the nTi-MOF device were found to be 16.41% and 15.52% for backward and forward sweeps, respectively. This indicates that the pristine nTi-MOF ETLs work efficiently to transfer electrons from the perovskite. It should be noted that the PCE of nTi-MOF device even without PCBM is significantly higher than that of all solar cell devices as developed using MOFs (3–13%).³¹ As the nTi-MOF ETLs become thicker, the device performance is gradually degraded by the reduction of their conductivity. For

the 20, 40, and 60 nm-thick nTi-MOF ETLs, the PCEs were found to be 16.41%, 13.82%, and 12.35%, respectively (Table S1). For the extremely thin nTi-MOF ETL (\sim 10 nm), a number of pinholes were generated, and the perovskite was directly contacted to ITO. This led to the significant degradation of the device performance, exhibiting a PCE of 9.98% (Figure S11).

The nTi-MOF/PCBM ETL significantly improved these PCEs up to 18.94% and 18.58% for backward and forward sweeps, respectively. For the backward sweeps, the open-circuit voltage (V_{oc}) increased from 1.066 to 1.082 V, short-circuit current density (J_{sc}) increased from 22.57 mA cm $^{-2}$ to 23.18 mA cm $^{-2}$, and fill factor (FF) increased from 0.682 to 0.755. The steady-state photocurrent densities of both devices were obtained at the maximum power voltage (V_{max} , 0.829 and 0.874 V for the nTi-MOF and nTi-MOF/PCBM device, respectively) (Figure S12). The obtained PCEs of the devices (16.22% and 18.63%) corresponded to those obtained from $J-V$ curves, which corroborated the excellent stability and performance under actual working conditions. This suggests that the combination of nTi-MOF and PCBM in ETLs has a synergetic effect on device performance and suppresses $J-V$ hysteresis. Further, the incorporation of PCBM into the nTi-MOF ETLs leads to better band alignment and reduces the contact resistance at the interfaces accompanying the facilitation of electron transfer, as shown in Figure 4b. Considering the highest PCE using bare PCBM ever reported was 15.30%,³³ nTi-MOF played a critical role with the help of PCBM to give the excellent device performance. We also prepared 50 nm-thick TiO₂ ETLs treated at 500 °C (HT-TiO₂) and then fabricated HT-TiO₂ and HT-TiO₂/PCBM devices under the same conditions of nTi-MOF and nTi-MOF/PCBM devices. The PCEs for HT-TiO₂ and HT-TiO₂/PCBM devices were 14.15% and 15.82%, respectively (Figure S13). Further, the photostability of the HT-TiO₂/PCBM and nTi-MOF/PCBM devices was investigated for 24 h under 1 sun illumination. At a relative humidity of 60%, the normalized PCEs of the HT-TiO₂/PCBM and nTi-MOF/PCBM devices decreased to 0.72 and 0.87 after 24 h, respectively (Figure S14). The enhanced photostability of the nTi-MOF/PCBM device was mainly attributed to the suppressed photocatalytic effect of the nTi-MOF on PCBM and perovskite.³⁴ The wider band gap of nTi-MOF (3.70 eV) than that of HT-TiO₂ (3.55 eV) led to the less absorbance of UV as shown in Figure S6, which contributed to the enhanced photostability of the surrounding layers. The significantly higher PCEs and photostability for nTi-MOF and nTi-MOF/PCBM devices clearly show the advantage of nTi-MOF ETL for high-performance PSCs.

The effects of nTi-MOF and PCBM layers were observed by the time-resolved photoluminescence (TRPL) spectroscopy results. Figure 4d exhibits the PL decay transients and the corresponding PL lifetimes in three samples of the glass/perovskite, glass/nTi-MOF/perovskite, and glass/nTi-MOF/PCBM/perovskite. These were obtained by fitting a biexponential decay function. The fitted parameters for the samples are summarized in Table S2. The fast decay corresponds to the quenching of charge carriers between the perovskite and the ETLs, while the slow decay is due to radiative decay within the perovskite film.^{35–37} The average PL lifetimes (τ) were found to be 24.63, 3.09, and 1.72 ns for the glass/perovskite, glass/nTi-MOF/perovskite, and glass/nTi-MOF/PCBM/perovskite, respectively. The shorter PL lifetimes for the glass/nTi-MOF/PCBM/perovskite suggest that the charge injection from the

perovskite to the nTi-MOF/PCBM became dominant. Thereby, the faster electron transfer suppresses the charge recombination, which improved the device parameters and the hysteresis behavior.^{38,39} Figure 4e presents the external quantum efficiency (EQE) spectra of the nTi-MOF and nTi-MOF/PCBM device. The slightly higher EQE values of the nTi-MOF/PCBM device than those of the nTi-MOF device were observed at wavelengths from 400 to 750 nm, since the PCBM layer efficiently suppressed the charge recombination by avoiding the direct contact between the perovskite and ITO.⁴⁰ The integrated J_{sc} from the EQE spectra exhibited an excellent agreement with the J_{sc} obtained from the $J-V$ curves. These were found to be 21.88 mA cm $^{-2}$ and 22.43 mA cm $^{-2}$ for the nTi-MOF and nTi-MOF/PCBM devices, respectively. Figure 4f shows the high reproducibility of the device performance across 20 devices. The average PCE was found to be 18.37% (with minimum and maximum values of 17.75% and 18.94%, respectively). The device parameters for the nTi-MOF and nTi-MOF/PCBM devices are summarized in Table 1.

Table 1. Photovoltaic Parameters of Rigid PSCs Measured under Standard AM 1.5 G Illumination of 100 mW cm $^{-2}$

ETL	scan direction	V_{oc} (V)	J_{sc} (mA cm $^{-2}$)	FF	PCE (%)
nTi-MOF	backward	1.066	22.47	0.682	16.41
	forward	1.052	22.32	0.661	15.52
nTi-MOF/PCBM	backward	1.082	23.18	0.755	18.94
	forward	1.081	23.16	0.742	18.58

The deposition process of nTi-MOF does not require thermal annealing. Therefore, nTi-MOF ETLs are highly suitable for use on plastic substrates. Figure 5a exhibits $J-V$ curves for flexible devices employing the nTi-MOF/PCBM ETL. The inset shows a bending image of the real device. Before bending, an excellent PCE of 17.43% was found (V_{oc} = 1.05 V, J_{sc} = 22.61 mA cm $^{-2}$, and FF = 0.734). In case of the PCBM device (*i.e.*, absence of nTi-MOFs in the ETL), a PCE was found to be 14.14% when ITO was treated with polyethylenimine-ethoxylated (PEIE). This was achieved by an increase in the work function of ITO from -4.7 eV to -4.0 eV. The resulting band alignment between the PCBM and ITO lowered the electron injection barrier, and charge transfer was facilitated at the interface.¹⁰ Without surface treatment of ITO, the PCE significantly dropped to 6.38% due to the high electron injection barrier (Figure S15). Therefore, the nTi-MOFs are of a highly efficient ETL of flexible PSCs.

This value was approximately retained up to a bending radius (r) of 10 mm (PCE = 16.96%). At r = 6 mm, the slight plastic deformation of the ITO/PEN substrate was observed. This led to a reduction of the initial PCE to 14.85%. The significant mechanical stress at r = 3 mm broke the ITO layer and caused a breakdown or severe degradation of the device performance (PCE = 4.31%). This durability test was performed on two devices at r = 10 mm and 6 mm, for up to 700 bending cycles (Figure 5b). The initial PCEs of 17.37% and 17.28% decreased to 15.43% and 11.73% after 700 bending cycles, respectively. As shown in Figure 5b, after the device was deformed once, the device performance decreased linearly at the same bending radius. Figure 5c presents the EQE spectra of the best-performing device. High EQE values were observed in the visible range, and the integrated J_{sc} was found to be 21.53 mA cm $^{-2}$. The histogram in Figure 5d shows the high

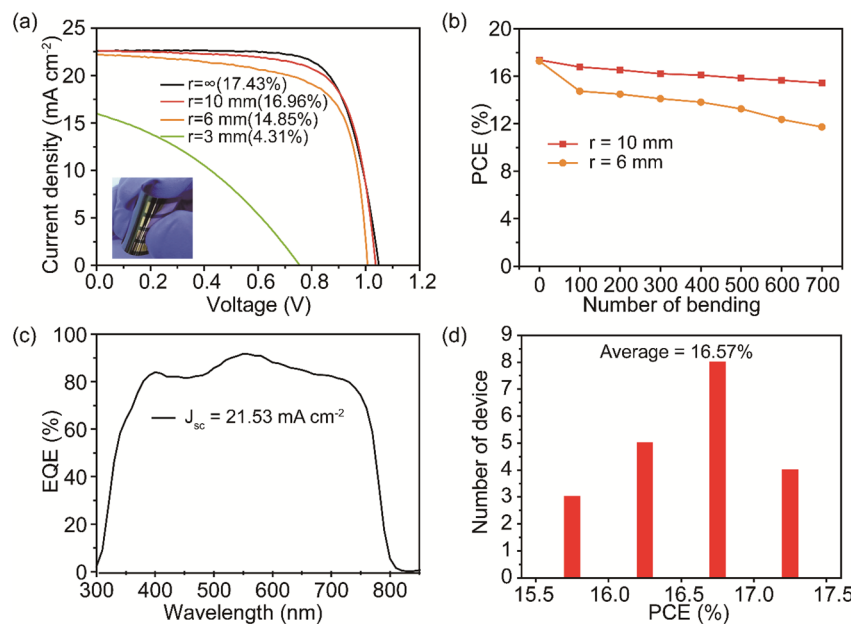


Figure 5. Characterization of the flexible nTi-MOF/PCBM PSCs. (a) $J-V$ curves of the flexible devices measured from $r = \infty$ to $r = 3\text{ mm}$. (b) Bending test of the devices for $r = 10\text{ mm}$ and $r = 6\text{ mm}$ up to 700 bending cycles. (c) EQE spectra of the best-performing device. (d) Histogram of the PCEs for 20 devices.

reproducibility of device performance. Twenty devices have an average PCE of 16.57% (with minimum and maximum values of 15.68% and 17.43%, respectively). The device parameters for the flexible device at different bending radius are summarized in Table S3.

CONCLUSIONS

In conclusion, we successfully synthesized the nanocrystalline nTi-MOF (*ca.* 6 nm) and used it to produce an efficient ETL in PSCs. The nTi-MOFs were highly dispersed in organic solvents, which led to the simple fabrication of uniform and ultrathin films. The electronic structure of nTi-MOFs was suitable for the transportation of electrons generated in the perovskite layer of the PSCs. The incorporation of PCBM into the nTi-MOF ETLs improved the film conductivity as well as suppressed the direct contact between the perovskite and substrates. These thus provide excellent device performance for both rigid (PCE = 18.94%) and flexible (PCE = 17.43%) PSC architectures. Further, the outstanding durability of the device was retained in up to 700 bending cycles, exhibiting a PCE of 15.43%. These results suggest that the nTi-MOF has great potential for use in the design of highly flexible architecture in PSCs and will result in excellent device performance. Solution-based printing techniques, such as roll-to-roll printing, spray printing, and bar-coating processes, would provide a highly efficient means of fabricating large-area, flexible devices using nTi-MOF.

MATERIALS AND METHODS

Materials. The following materials were purchased from Sigma-Aldrich: 1,4-benzenedicarboxylic acid (H_2BDC , 98%), titanium(IV) butoxide (97%), anhydrous dimethylformamide (DMF, 99.8%), anhydrous methanol (99.8%), bis(trifluoromethane) sulfonamide lithium salt (Li-TFSI, 99.95%), anhydrous acetonitrile (ACN, 99.8%), anhydrous dimethyl sulfoxide (DMSO, 99.9%), anhydrous dimethylformamide (DMF, 99.8%), anhydrous diethyl ether (99.9%), 4-*tert*-butylpyridine (*t*Bp, 96%), anhydrous chlorobenzene (CB, 99.8%), [6,6]-phenyl C₆₁ butyric acid methyl ester (PCBM,

>99.5%), polyethylenimine-ethoxylated solution (PEIE, 35–40 wt % in H₂O), and anhydrous 2-methoxyethanol (99.8%). TiO₂ paste (particle size = 20 nm) was purchased from NanoPac. PbI₂ (99.9985%) was purchased from Alfa Aesar. Methylammonium iodide (MAI) and formamidinium iodide (FAI) were purchased from Dyesol. Spiro-MeOTAD was purchased from Merck. The CH₃NH₃PbI₃ precursor solution was prepared *via* the Lewis base adduct approach according to a previous report; 1 M of PbI₂, 0.95 M of MAI, 0.05 M of FAI, and 78 mg of DMSO were mixed with 600 mg of DMF.

Synthesis of nTi-MOF. 1,4-Benzenedicarboxylic acid (H_2BDC , 0.25 g, 1.5 mmol) was dissolved in anhydrous dimethylformamide (DMF, 9 mL) and methanol (1 mL), in a 20 mL glass vial. Titanium(IV) butoxide (0.13 mL, 0.37 mmol) was then added into the well-dissolved solution. The mixture was stirred at room temperature until the solution turned transparent. Then, the sealed vial was placed in a 150 °C aluminum heating block for 15 h. After the reaction, it was cooled to room temperature, and the solid was separated with a centrifuge (9000 rpm for 10 min), followed by washing with DMF and methanol. The resulting product was filtered using a GF/A glass fiber filter papers (Whatman) to give size-uniformity and then dispersed in 2-butanol to make an nTi-MOF colloidal solution (8 mg/mL).

Fabrication of Perovskite Solar Cells. The nTi-MOF solution (8 mg/mL in 2-butanol) was treated with UV/O₃ for 15 min. It was then spin-coated onto the patterned ITO/glass or ITO/PEN substrates (dimension = 2.5 cm × 2.5 cm) at 3000 rpm for 30 s. For surface treatment of ITO with PEIE, 0.2 wt % of PEIE solution diluted with 2-methoxyethanol was spin-coated onto the substrates at 6000 rpm for 60 s. The perovskite precursor solution was spin-coated onto the nTi-MOF ETL at 4000 rpm for 25 s and 0.5 mL of diethyl ether was dripped, for 10 s, on the rotating sample. This sample was then heated at 65 °C for 1 min and at 135 °C for a further 1 min. The spiro-MeOTAD solution, consisting of 56 mg of spiro-MeOTAD, 5.6 mg of Li-TFSI, and 30 mg of *t*Bp in 1 mL CB, was spin-coated onto the perovskite layer at 2500 rpm for 20 s. Finally, an Au electrode was deposited at a constant rate of 0.5 Å using a thermal evaporator.

Characterization. The powder X-ray diffraction spectra were obtained using a RIGAKU XRD (Smartlab, Cu-K α radiation) at 1200 W (40 kV, 30 mA). The scanning condition was set to a 4°/min scan rate from 5° to 40°, using a silicon holder. The morphology and surface of the MOFs were verified using a field emission scanning electron microscope (FE-SEM, JEM-7600F, JEOL). Focused ion beam

(FIB) was performed with a Quanta3D FEG (FEI Company). Transmission electron microscopy (TEM) was carried out at 200 kV using a JEOL JEM-2100F. The X-ray photoelectron spectroscopy (XPS, AXIS SUPRA, Kratos) was conducted using Al-K α radiation with a 15 kV, 375 W X-ray source, and a 400 μ m beam size. The ultraviolet photoelectron spectroscopy (UPS, AXIS SUPRA, Kratos) was performed under a He I source with a 21.22 eV photoemission energy and a -9.0 V sample bias. Gas adsorption analysis was performed using a BELSOPR-max (MicrotracBEL Corp.) gas adsorption analyzer. Samples were prepared and measured after evacuating at 120 °C for 24 h. Time-resolved PL measurements were performed at the PL maxima of the perovskite (770 nm), using a time-correlated single photon counting module (TCSPC, MPD-PDM Series DET-40 photon counting detector and Pendulum CNT-91 frequency counter). This module was combined with a monochromator and a second-harmonic-generated 400 nm laser, derived from an 800 nm Ti:sapphire laser (Mai Tai, Spectra-Physics). These served as a detector and an excitation source, respectively. The I - V curves were obtained using an Agilent E5270A parametric measurement mainframe. The J - V curves were obtained using a Keithley model 2400 source meter unit. A 150 W xenon lamp in a solar simulator was used as the light source. The light intensity was adjusted to AM 1.5 G using a NREL-calibrated Si solar cell. The active area of 0.12 cm² was defined using a metal mask. The external quantum efficiency (EQE) spectra were generated using incident photon-to-current efficiency (IPCE) equipment (PV Measurement, Inc.).

ASSOCIATED CONTENT

Supporting Information

The Supporting Information is available free of charge on the ACS Publications website at DOI: [10.1021/acsnano.8b02079](https://doi.org/10.1021/acsnano.8b02079).

IR spectroscopy of Ti-MOF and nTi-MOF; N₂ adsorption-desorption isotherms for nTi-MOFs; transparency of nTi-MOF and mesoporous TiO₂ ETLs; SEM image of the nTi-MOF/PCBM ETL; I - V curves of the mesoporous TiO₂, nTi-MOF, and nTi-MOF/PCBM; SEM image of perovskite deposited onto the nTi-MOF/PCBM ETL; UV-vis spectra of the MAPbI₃ and (MAPbI₃)_{0.95}(FAPbI₃)_{0.05}; steady-state photocurrent densities of nTi-MOF and nTi-MOF/PCBM devices; PCEs of HT-TiO₂ and HT-TiO₂/PCBM compared with nTi-MOF and nTi-MOF/PCBM; TRPL parameters; photovoltaic parameters of a flexible PSC for various bending radii ([PDF](#))

AUTHOR INFORMATION

Corresponding Authors

*E-mail: mwpark@sookmyung.ac.kr.
*E-mail: kmchoi@sookmyung.ac.kr.

ORCID

UnJin Ryu: [0000-0002-4854-3587](https://orcid.org/0000-0002-4854-3587)

Joon-Suh Park: [0000-0002-3235-5450](https://orcid.org/0000-0002-3235-5450)

Kyung Min Choi: [0000-0001-7181-902X](https://orcid.org/0000-0001-7181-902X)

Notes

The authors declare no competing financial interest.

ACKNOWLEDGMENTS

This work was supported by the Basic Science Research Program through the National Research Foundation of Korea (NRF) funded by the Ministry of Science and ICT (2016R1C1B2011016 and 2016R1C1B1010781). M.P. was supported from Sookmyung Women's University Research Grant (1-1703-2015). K.M.C and U.R. were further supported from Sookmyung Women's University Research Grant (1-

1603-2037) and the Global Ph.D. Fellowship Program through NRF (2017H1A2A1044712), respectively.

REFERENCES

- (1) Kojima, A.; Teshima, K.; Shirai, Y.; Miyasaka, T. Organometal Halide Perovskites as Visible-Light Sensitizers for Photovoltaic Cells. *J. Am. Chem. Soc.* **2009**, *131*, 6050–6051.
- (2) Kim, H.-S.; Lee, C.-R.; Im, J.-H.; Lee, K.-B.; Moehl, T.; Marchioro, A.; Moon, S.-J.; Humphry-Baker, R.; Yum, J.-H.; Moser, J. E.; Grätzel, M.; Park, N.-G. Lead Iodide Perovskite Sensitized All-Solid-State Submicron Thin Film Mesoscopic Solar Cell with Efficiency Exceeding 9%. *Sci. Rep.* **2012**, *2*, 591.
- (3) Burschka, J.; Pellet, N.; Moon, S.-J.; Humphry-Baker, R.; Gao, P.; Nazeeruddin, M. K.; Grätzel, M. Sequential Deposition as a Route to High-Performance Perovskite-Sensitized Solar Cells. *Nature* **2013**, *499*, 316–319.
- (4) National Renewable Energy Laboratory, *Best Research-Cell Efficiencies*, <https://www.nrel.gov/pv/assets/images/efficiency-chart.png> (accessed January 4, 2018).
- (5) Park, M.; Kim, H. J.; Jeong, I.; Lee, J.; Lee, H.; Son, H. J.; Kim, D.-E.; Ko, M. J. Flexible Solar Cells: Mechanically Recoverable and Highly Efficient Perovskite Solar Cells: Investigation of Intrinsic Flexibility of Organic-Inorganic Perovskite. *Adv. Energy Mater.* **2015**, *5*, 1501406.
- (6) Sun, S.; Fang, Y.; Kieslich, G.; White, T. J.; Cheetham, A. K. Mechanical Properties of Organic-Inorganic Halide Perovskites, CH₃NH₃PbX₃ (X = I, Br and Cl), by Nanoindentation. *J. Mater. Chem. A* **2015**, *3*, 18450–18455.
- (7) Park, M.; Kim, J.-Y.; Son, H. J.; Lee, C.-H.; Jang, S. S.; Ko, M. J. Low-Temperature Solution-Processed Li-doped SnO₂ as an Effective Electron Transporting Layer for High-Performance Flexible and Wearable Perovskite Solar Cells. *Nano Energy* **2016**, *26*, 208–215.
- (8) Di Giacomo, F.; Zardetto, V.; D'Epifanio, A.; Pescetelli, S.; Matteocci, F.; Razza, S.; Di Carlo, A.; Licoccia, S.; Kessels, W. M. M.; Creatore, M.; Brown, T. M. Flexible Perovskite Photovoltaic Modules and Solar Cells Based on Atomic Layer Deposited Compact Layers and UV-Irradiated TiO₂ Scaffolds on Plastic Substrates. *Adv. Energy Mater.* **2015**, *5*, 1401808.
- (9) Yang, D.; Yang, R.; Ren, X.; Zhu, X.; Yang, Z.; Li, C.; Liu, S. Hysteresis-Suppressed High-Efficiency Flexible Perovskite Solar Cells Using Solid-State Ionic-Liquids for Effective Electron Transport. *Adv. Mater.* **2016**, *28*, 5206–5213.
- (10) Park, M.; Park, J.-S.; Han, I. K.; Oh, J. Y. High-Performance Flexible and Air-Stable Perovskite Solar Cells with a Large Active Area Based on Poly(3-hexylthiophene) Nanofibrils. *J. Mater. Chem. A* **2016**, *4*, 11307–11316.
- (11) Jo, J. W.; Seo, M.-S.; Park, M.; Kim, J.-Y.; Park, J. S.; Han, I. K.; Ahn, H.; Jung, J. W.; Sohn, B.-H.; Ko, M. J.; Son, H. J. Improving Performance and Stability of Flexible Planar-Heterojunction Perovskite Solar Cells Using Polymeric Hole-Transport Material. *Adv. Funct. Mater.* **2016**, *26*, 4464–4471.
- (12) Kim, B. J.; Kim, D. H.; Lee, Y.-Y.; Shin, H.-W.; Han, G. S.; Hong, J. S.; Mahmood, K.; Ahn, T. K.; Joo, Y.-C.; Hong, K. S.; Park, N.-G.; Lee, S.; Jung, H. S. Highly Efficient and Bending Durable Perovskite Solar Cells: Toward a Wearable Power Source. *Energy Environ. Sci.* **2015**, *8*, 916–921.
- (13) Yang, D.; Yang, R.; Zhang, J.; Yang, Z.; Liu, S.; Li, C. High Efficiency Flexible Perovskite Solar Cells Using Superior Low Temperature TiO₂. *Energy Environ. Sci.* **2015**, *8*, 3208–3214.
- (14) Jeong, I.; Jung, H.; Park, M.; Park, J. S.; Son, H. J.; Joo, J.; Lee, J.; Ko, M. J. A Tailored TiO₂ Electron Selective Layer for High-Performance Flexible Perovskite Solar Cells via Low Temperature UV Process. *Nano Energy* **2016**, *28*, 380–389.
- (15) You, J.; Meng, L.; Song, T.-B.; Guo, T.-F.; Yang, Y. M.; Chang, W.-H.; Hong, Z.; Chen, H.; Zhou, H.; Chen, Q.; Liu, Y.; De Marco, N.; Yang, Y. Improved Air Stability of Perovskite Solar Cells via Solution-Processed Metal Oxide Transport Layers. *Nat. Nanotechnol.* **2016**, *11*, 75–81.

- (16) Shin, S. S.; Yeom, E. J.; Yang, W. S.; Hur, S.; Kim, M. G.; Im, J.; Seo, J.; Noh, J. H.; Seok, S. I. Colloidally Prepared La-Doped BaSnO₃ Electrodes for Efficient, Photostable Perovskite Solar Cells. *Science* **2017**, *356*, 167–171.
- (17) Kim, J. H.; Liang, P.-W.; Williams, S. T.; Cho, N.; Chueh, C.-C.; Glaz, M. S.; Ginger, D. S.; Jen, A. K. -Y. High-Performance and Environmentally Stable Planar Heterojunction Perovskite Solar Cells Based on a Solution-Processed Copper-Doped Nickel Oxide Hole-Transporting Layer. *Adv. Mater.* **2015**, *27*, 695–701.
- (18) Jung, J. W.; Chueh, C.-C.; Jen, A. K. -Y. A Low-Temperature, Solution-Processable, Cu-Doped Nickel Oxide Hole-Transporting Layer *via* the Combustion Method for High-Performance Thin-Film Perovskite Solar Cells. *Adv. Mater.* **2015**, *27*, 7874–7880.
- (19) Zhang, H.; Cheng, J.; Lin, F.; He, H.; Mao, J.; Wong, K. S.; Jen, A. K. -Y.; Choy, W. C. H. Pinhole-Free and Surface-Nanostructured NiO_x Film by Room-Temperature Solution Process for High-Performance Flexible Perovskite Solar Cells with Good Stability and Reproducibility. *ACS Nano* **2016**, *10*, 1503–1511.
- (20) Shin, S. S.; Yang, W. S.; Yeom, E. J.; Lee, S. J.; Jeon, N. J.; Joo, Y.-C.; Park, I. J.; Noh, J. H.; Seok, S. I. Tailoring of Electron-Collecting Oxide Nanoparticulate Layer for Flexible Perovskite Solar Cells. *J. Phys. Chem. Lett.* **2016**, *7*, 1845–1851.
- (21) Tan, H.; Jain, A.; Voznyy, O.; Lan, X.; Garcia de Arquer, F. P.; Fan, J. Z.; Quintero-Bermudez, R.; Yuan, M.; Zhang, B.; Zhao, Y.; Fan, F.; Li, P.; Quan, L. N.; Zhao, Y.; Lu, Z.-H.; Yang, Z.; Hoogland, S.; Sargent, E. H. Efficient and Stable Solution-Processed Planar Perovskite Solar Cells *via* Contact Passivation. *Science* **2017**, *355*, 722–726.
- (22) Das, S.; Gu, G.; Joshi, P. C.; Yang, B.; Aytug, T.; Rouleau, C. M.; Geohegan, D. B.; Xiao, K. Low Thermal Budget, Photonic-Cured Compact TiO₂ Layers for High-Efficiency Perovskite Solar Cells. *J. Mater. Chem. A* **2016**, *4*, 9685–9690.
- (23) Feleki, B.; Bex, G.; Andriessen, R.; Galagan, Y.; Di Giacomo, F. Rapid and Low Temperature Processing of Mesoporous TiO₂ for Perovskite Solar Cells on Flexible and Rigid Substrates. *Mater. Today Commun.* **2017**, *13*, 232–240.
- (24) Furukawa, H.; Cordova, K. E.; O'Keeffe, M.; Yaghi, O. M. The Chemistry and Applications of Metal-Organic Frameworks. *Science* **2013**, *341*, 1230444.
- (25) Choi, K. M.; Jeong, H. M.; Park, J. H.; Zhang, Y.-B.; Kang, J. K.; Yaghi, O. M. Supercapacitors of Nanocrystalline Metal–Organic Frameworks. *ACS Nano* **2014**, *8*, 7451–7457.
- (26) Dan-Hardi, M.; Serre, C.; Frot, T.; Rozes, L.; Maurin, G.; Sanchez, C.; Férey, G. A New Photoactive Crystalline Highly Porous Titanium (IV) Dicarboxylate. *J. Am. Chem. Soc.* **2009**, *131*, 10857–10859.
- (27) Hendon, C. H.; Tiana, D.; Fontecave, M.; Sanchez, C.; D'arras, L.; Sasso, C.; Rozes, L.; Mellot-Draznieks, C.; Walsh, A. Engineering the Optical Response of the Titanium-MIL-125 Metal–Organic Framework Through Ligand Functionalization. *J. Am. Chem. Soc.* **2013**, *135*, 10942–10945.
- (28) Fu, Y.; Sun, D.; Chen, Y.; Huang, R.; Ding, Z.; Fu, X.; Li, Z. An Amine-Functionalized Titanium Metal–Organic Framework Photocatalyst with Visible-Light-Induced Activity for CO₂ Reduction. *Angew. Chem.* **2012**, *124*, 3420–3423.
- (29) Chang, T.-S.; Kung, C.-W.; Chen, H.-W.; Huang, T.-Y.; Kao, S.-Y.; Lu, H.-C.; Lee, M.-H.; Boopathi, K. M.; Chu, C.-W.; Ho, K.-C. Planar Heterojunction Perovskite Solar Cells Incorporating Metal–Organic Framework Nanocrystals. *Adv. Mater.* **2015**, *27*, 7229–7235.
- (30) Vinogradov, A. V.; Zaake-Hertling, H.; Hey-Hawkins, E.; Agafonov, A. V.; Seisenbaeva, G. A.; Kessler, V. G.; Vinogradov, V. V. The First Depleted Heterojunction TiO₂-MOF-Based Solar Cell. *Chem. Commun.* **2014**, *50*, 10210–10213.
- (31) Kaur, R.; Kim, K.-H.; Paul, A.; Deep, A. Recent Advances in the Photovoltaic Applications of Coordination Polymers and Metal Organic Frameworks. *J. Mater. Chem. A* **2016**, *4*, 3991–4002.
- (32) Ahn, N.; Son, D.-Y.; Jang, I.-H.; Kang, S. M.; Choi, M.; Park, N.-G. Highly Reproducible Perovskite Solar Cells with Average Efficiency of 18.3% and Best Efficiency of 19.7% Fabricated *via* Lewis Base Adduct of Lead (II) Iodide. *J. Am. Chem. Soc.* **2015**, *137*, 8696–8699.
- (33) Ryu, S.; Seo, J.; Shin, S. S.; Kim, Y. C.; Jeon, N. J.; Noh, J. H.; Seok, S. I. Fabrication of Metal-Oxide-Free CH₃NH₃PbI₃ Perovskite Solar Cells Processed at Low Temperature. *J. Mater. Chem. A* **2015**, *3*, 3271–3275.
- (34) Yoon, S.; Kim, S. J.; Kim, H. S.; Park, J.-S.; Han, I. K.; Jung, J. W.; Park, M. Solution-Processed Indium Oxide Electron Transporting Layers for High-Performance and Photo-Stable Perovskite and Organic Solar Cells. *Nanoscale* **2017**, *9*, 16305–16312.
- (35) deQuilettes, D. W.; Vorpahl, S. M.; Stranks, S. D.; Nagaoka, H.; Eperon, G. E.; Ziffer, M. E.; Snaith, H. J.; Ginger, D. S. Impact of Microstructure on Local Carrier Lifetime in Perovskite Solar Cells. *Science* **2015**, *348*, 683–686.
- (36) Liang, P.-W.; Liao, C.-Y.; Chueh, C.-C.; Zuo, F.; Williams, S. T.; Xin, X.-K.; Lin, J.; Jen, A. K. -Y. Additive Enhanced Crystallization of Solution-Processed Perovskite for Highly Efficient Planar-Heterojunction Solar Cells. *Adv. Mater.* **2014**, *26*, 3748–3754.
- (37) Zuo, L.; Gu, Z.; Ye, T.; Fu, W.; Wu, G.; Li, H.; Chen, H. Enhanced Photovoltaic Performance of CH₃NH₃PbI₃ Perovskite Solar Cells through Interfacial Engineering Using Self-Assembling Monolayer. *J. Am. Chem. Soc.* **2015**, *137*, 2674–2679.
- (38) Jung, J. W.; Park, J.-S.; Han, I. K.; Lee, Y.; Park, C.; Kwon, W.; Park, M. Flexible and Highly Efficient Perovskite Solar Cells with a Large Active Area Incorporating Cobalt-Doped Poly(3-hexylthiophene) for Enhanced Open-Circuit Voltage. *J. Mater. Chem. A* **2017**, *5*, 12158–12167.
- (39) Li, Y.; Zhao, Y.; Chen, Q.; Yang, Y. M.; Liu, Y.; Hong, Z.; Liu, Z.; Hsieh, Y.-T.; Meng, L.; Li, Y.; Yang, Y. Multifunctional Fullerene Derivative for Interface Engineering in Perovskite Solar Cells. *J. Am. Chem. Soc.* **2015**, *137*, 15540–15547.
- (40) Aharon, S.; Cohen, B. E.; Etgar, L. Hybrid Lead Halide Iodide and Lead Halide Bromide in Efficient Hole Conductor Free Perovskite Solar Cell. *J. Phys. Chem. C* **2014**, *118*, 17160–17165.